minerals

MDPI

Article

The Role of Organic Matter on Uranium Precipitation in Zoovch Ovoo, Mongolia

Dimitrios Rallakis [1], Raymond Michels [1,*], Marc Brouand [2], Olivier Parize [2] and Michel Cathelineau [1,*]

[1] GeoRessources Laboratory, Université de Lorraine, CNRS, CREGU, rue Jacques Callot, F-54506 Vandoeuvre-lès-Nancy, France; dimitrios.rallakis@univ-lorraine.fr

[2] ORANO Mining, Tour AREVA, place Jean Millier 1, 92084 Courbevoie, France; marc.brouand@orano.group (M.B.); olivier.parize@orano.group (O.P.)

* Correspondence: raymond.michels@univ-lorraine.fr (R.M.); michel.cathelineau@univ-lorraine.fr (M.C.); Tel.: +33-372-745-561 (R.M.); +33-372-745-543 (M.C.)

Received: 10 April 2019; Accepted: 14 May 2019; Published: 18 May 2019

Abstract: The Zoovch Ovoo uranium deposit is located in East Gobi Basin in Mongolia. It is hosted in the Sainshand Formation, a Late Cretaceous siliciclastic reservoir, in the lower part of the post-rift infilling of the Mesozoic East Gobi Basin. The Sainshand Formation corresponds to poorly consolidated medium-grained sandy intervals and clay layers deposited in fluvial-lacustrine settings. The uranium deposit is confined within a 60- to 80-m-thick siliciclastic reservoir inside aquifer driven systems, assimilated to roll-fronts. As assessed by vitrinite reflectance (%Rr < 0.4) and molecular geochemistry, the formation has never experienced significant thermal maturation. Detrital organic matter (type III and IV kerogens) is abundant in the Zoovch Ovoo depocenter. In this framework, uranium occurs as: (i) U-rich macerals without any distinguishable U-phase under SEM observation, containing up to 40 wt % U; (ii) U expressed as UO_2 at the rims of large (several millimeters) macerals and (iii) U oxides partially to entirely replacing macerals, while preserving the inherited plant texture. Thus, uranium is accumulated gradually in the macerals through an organic carbon–uranium epigenization process, in respect to the maceral's chemistry and permeability. Most macerals are rich in S and, to a lesser extent, in Fe. Frequently, Fe and S contents do not fit the stoichiometry of pyrite, although pyrite also occurs as small inclusions within the macerals. The organic matter appears thus as a major redox trap for uranium in this kind of geological setting.

Keywords: roll-front; uranium; organic matter; late cretaceous; East Gobi Basin; Mongolia

1. Introduction

Organic carbon is considered an important uranium reducer in sedimentary uranium ore deposits [1–6]. Several mechanisms may account for uranium fixation by low maturity lignite and reduction during its burial history. It is possible for uranium to be adsorbed by carboxyl groups, and form organo-uranyl compounds, by means of cation exchange at ambient conditions, or without cation exchange when exposed to heat [7]. However, adsorption may not be accompanied by U(VI) reduction [8–10]. With increasing thermal maturity, U adsorption may co-exist with reduction reactions. At higher temperatures [11,12] reduction of U(VI) is predominant.

It is therefore proposed that, in geological environments, U may be trapped by peat or lignite without reduction at low temperatures (lignite stage [13,14]), while at later diagenetic stages (catagenesis, metagenesis stages of coalification) U reduction will prevail. The reduction mechanism of U(VI) may occur through the dehydrogenation of aliphatic and hydroxyl hydrocarbonaceous moieties [7,9]. As a result, two protons (H^+) are liberated from the organic matter, and two oxygens are fixed

during the formation of UO_2 [12,15,16]. Roll-front systems are ideal environments to study organic matter–uranium relationships as uranium and iron–sulfur bearing phases are dissolved and then re-precipitated along a physical–chemical front that progressively affects sands or sandstones that are frequently rich in detrital organic matter [17,18]. Central Asia has three important roll-front provinces: (i) the Chu-Sarysu basin in Southern Kazakhstan, where a large-scale U roll-front system of tens of kilometers is exploited [19–21]; (ii) the Yili, Tuha, Ordos and Erlian basins in North-East and North China [22–25]; and (iii) the East Gobi Basin in Mongolia, with the Zoovch Ovoo and Dulaan Uul U-ore deposits [26]. The Zoovch Ovoo deposit provides a unique opportunity to study organic matter–uranium relationships, as the host formation is richer in organic matter than most other deposits. The macerals were studied in detail, with particular focus on the textural relationships with uranium phases and sulfides, as well as on the spatial distribution of U, Fe and S in maceral grains. The objective was to understand the role of organic matter in uranium trapping and reduction.

2. Geological Setting

The roll-front system of the Zoovch Ovoo U-ore deposit is hosted in the Cenomanian Sainshand Formation of which the thickness ranges from 100 to 350 m [26]. The system can be separated into respective sub-units that reflect different cycles of lacustrine and alluvial sedimentation, resulting in an association of conglomerates, sands, silts and clays [27]. In particular, the sand dunes of the flood-dominated braided delta inside the lacustrine realm serve as uranium reservoirs (Figure 1). The Sainshand Formation is overlaid by the Late Cretaceous (Turonian–Santonian) Bayanshiree Formation, consisting mainly of reddish to greyish shales with minor input of sandstones of meandering channel-shape geometry [26,28,29]. The Late Cretaceous lacustrine coarse clastic units, namely the Santonian–Campanian Baruungoyot Formation and the Campanian–Maastrichtian Nemegt Formation only occur sporadically. Finally, Tertiary and Quaternary sediments are undifferentiated with granular sizes from very fine to coarse, unconformably topping the Late Cretaceous strata [30].

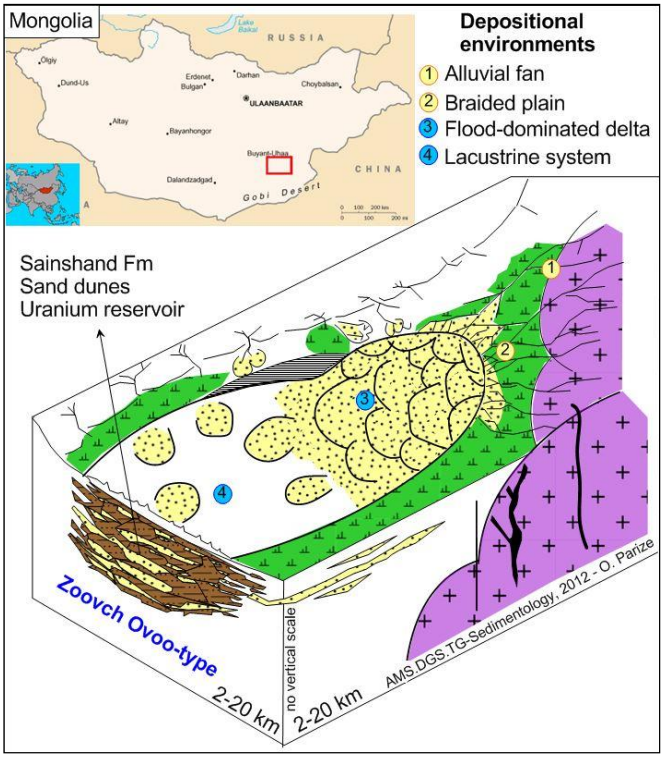

Figure 1. Location map of the study area and depositional model of the Zoovch Ovoo depocenter in the Cenomanian [26]. The sedimentary depositional systems are fluvio-lacustrine with alluvial fans, braided rivers and deltas. The sands of the Sainshand Formation host uranium mineralization.

3. Materials and Methods

The current study was carried out on core samples recovered during the exploration campaigns conducted by COGEGOBI, from 2011 to 2017, in Zoovch Ovoo. Samples were recovered in the roll-front area within the Sainshand Formation at the depths shown in Figure 2. Coal layers are lacking inside the reservoir zone and organic matter occurs at random as detrital particles following sedimentary bedding. The coarse, angular and poorly sorted organic particles associated with fine to coarse grained sands are reworked sediments (intraclasts), linked to distant transport and high-energy depositional settings. On the other hand the organic matter particles encountered in fine clay (organic-rich) layers are better preserved and linked to low-energy depositional settings under less oxygenated conditions. The well-preserved phytoclasts, such as root remains associated with fine grained organic-rich lithofacies, could be indicative of higher plant remains that grew within the depositional environment setting and did not undergo any significant transport.

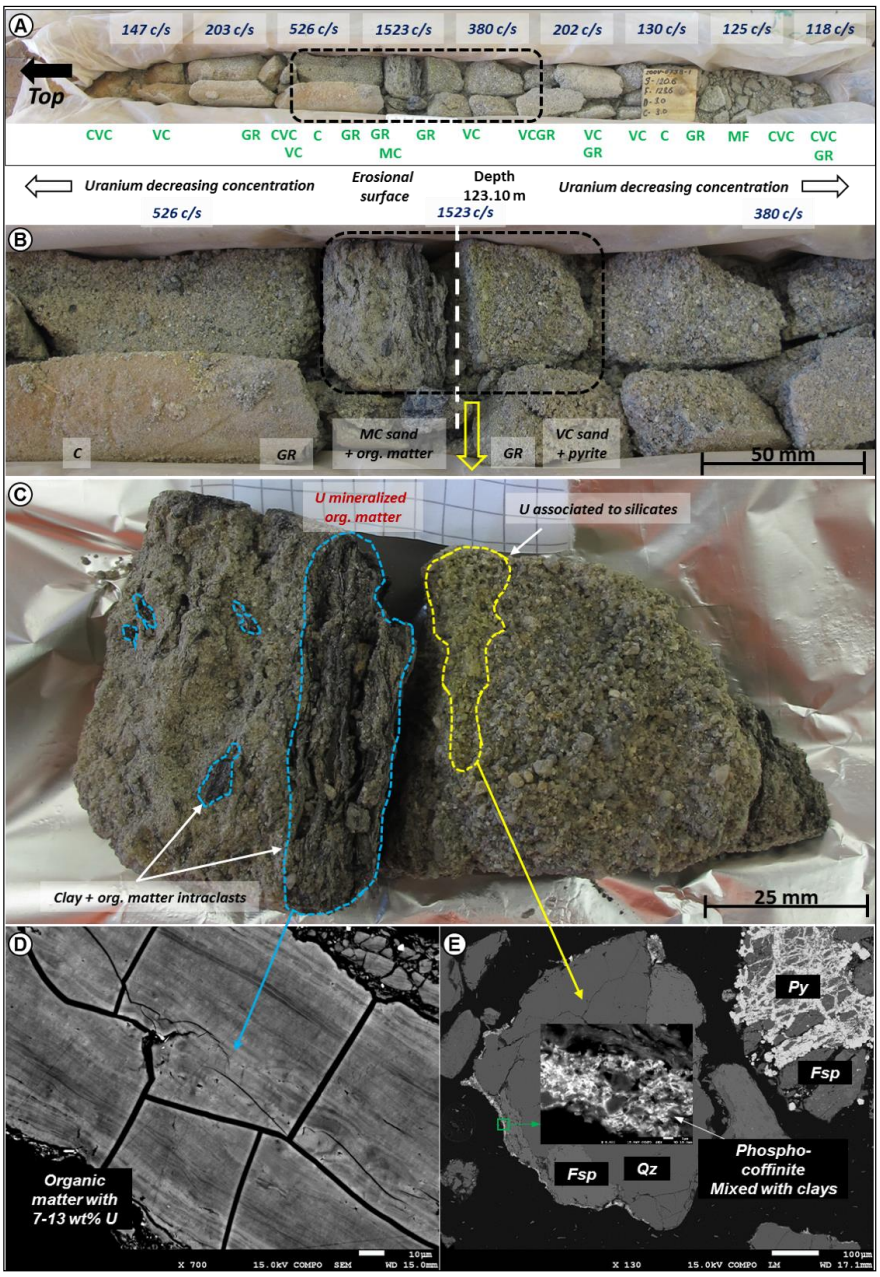

Figure 2. Abbreviations: GR (granules), CVC (coarse to very coarse sand), VC (very coarse sand), C (coarse sand), MC (medium coarse sand), Fsp (feldspar), Qz (quartz), Py (pyrite). (**A**) Drill-core

recovered from 123.20 m depth targeting the U reservoir, Sainshand Formation; Gamma ray spectroscopy measurements, presented in blue, were performed in contact with the rock unit with a step distance of 10 cm, expressed in c/s (counts per second). (**B**) Two upward-fining sequences are distinguished, starting with granules and ending with medium coarse sand in both cases. The sequences are separated by an erosional surface, followed by coarse deposits containing intraclasts of silty clay and organic matter. (**C**) A zoomed image of (B) highlighting the areas of organic matter and higher uranium concentration. The intense bright yellow color reveals an oxidation of U ores in contact with air. Uranium concentration is the highest at the contact with the erosional surface. (**D**) Organic matter particle containing 7–13 wt % uranium, without mineral expression. (**E**) Silicate grains coated by phospho-coffinite intermixed with clays. (D, E images under SEM/back-scattered electron mode.)

3.1. Petrography

3.1.1. Optical Microscopy

Polished thin sections (~30 µm thick) were studied using optical microscopy in transmitted and reflected light modes, with the objectives to describe the morphology and the nature of the different types of uranium mineralization encountered along the redox front.

3.1.2. Scanning Electron Microscopy

A Hitachi FEG S4800 high-resolution scanning electron microscope (SEM) (Tokyo, Japan) equipped with an energy dispersive spectrometer (EDS) using a Si-(Li) semi-conductor detector, coupled to a wavelength-dispersion spectrometer (WDS), was used in order to establish the mineral paragenesis and identify the main uranium bearing phases and their composition.

3.1.3. Organic Petrography

Polished blocks were prepared from the organic matter-rich samples and studied by means of oil-immersion petrography. The samples were initially screened for their organic matter content, either forming thin laminae following the sedimentary bedding, or as coal-rich clay intraclasts and phytoclasts (plant remains) inside the poorly consolidated sands, or as carbonate-cemented sandstones. Consequently, the organic matter was mechanically sorted and recovered from the sand and sandstone samples. The material was then grossly hand-crushed using an agate mortar, to prevent the production of fine-grained particles. The detailed methodology followed for the preparation of the polished blocks, as well as for polishing, was based on [31].

The random vitrinite reflectance (%Rr) was measured on polished blocks with a diameter of 1 mm, and were then mounted on epoxy resin according to ISO 7404-2 [32]. A Zeiss (Axio Imager D1M) microscope equipped with oil-immersion objectives with 50× magnification was used. The vitrinite reflectance was conducted following ISO 7404-5 [33]. The reflectance measurements were made on huminite using spinel (%R = 0.420) as a standard, and a photomultiplier tube (PMS) coupled to Spectra Vision A.S & Cosoftware (Version 2008, GmbH, Munich, Germany).

3.1.4. In Situ Analysis

The electron probe micro-analysis (EPMA) of uranium cements was performed using a CAMECA SX100 at SCMEM (Service Commun de Microscopie Electronique) Nancy. The calibration was made against natural and synthetic oxides or alloys (orthoclase, albite, $MnTiO_3$, wollastonite, hematite and olivine). The analytical conditions were: 10 nA current, 15 kV accelerating voltage, 10 s counting time for (K, Na, Ca), 20 s for (Al, Fe, Mn), 40 s for (Mg). The accelerating voltage was raised from 15 to 25 kV to amplify the detection limit, in particular when investigating the uranium–organic matter relationships.

3.1.5. Micro X-Ray Fluorescence Mapping

Micro-X-ray fluorescence (XRF) mapping was obtained using a M4 Tornado instrument (Bruker Nano GmbH, Berlin, Germany). The system has a Rh X-ray tube with a Be side window and polycapillary optics, which provides an X-ray beam with a diameter of 25–30 μm on the sample. The X-ray tube was operated at 50 kV and 200 μA. X-rays were detected by a 30 mm^2 xflash SDD with an energy resolution of <135 eV at 250,000 cps. All analyses were carried out at 2 kPa vacuum. Semi-quantitative maps were generated for major elements such as U, Fe, S and Ti.

4. Results

4.1. Organic Matter Sedimentology

Organic matter occurs as disseminated detrital particles (dispersed organic matter—DOM) within poorly consolidated coarse sand to clay lithologies. For instance, organic detrital particles can be found (1) dispersed within poorly sorted sand layers with no visible internal structure, (2) concentrated into laminae of well-structured fining upward layers or bottom sets of dunes/mega ripples, (3) associated with clay-rich intraclasts located at the base of sandy layers and (4) dispersed within silt to clay-rich layers.

Two typical samples of uranium-enriched layers are presented in Figure 2. Maximum SSPγ counts/second (1523 c/s) are recorded at the erosional surface located beneath a base of layer rich in organic matter and clay. SSPγ counts/second decrease downward or upward from this limit.

Uranium is concentrated inside underwater dune sediments (pebbles made of clay/detrital organic matter intraclasts, gravel and sand) that represent the base of the delta foreset slope. After burial, the oxidizing mineralized fluids advance through the well-sorted coarse sandy to microconglomeratic deposits. The high-energy depositional conditions during the formation of these sequences explain the absence of the fine fractions, which implies high permeability.

4.2. Organic Petrography

In organic petrography, the term vitrinite is used to distinguish between organic matter that has reached a certain coalification stage, in contrast with huminite, which refers to peat material of very low maturity and poor gelification. Hence, considering the petrographic features of the macerals, the low burial depth (<500 m) [30] and the very low vitrinite reflectance measurements in the Zoovch Ovoo sands (%Rr = 0.302 ± 0.02), it can be concluded that the type III kerogen never reached the thermal maturity needed to be accredited as vitrinite. Therefore, since the organic matter is still in the peat stage, the nomenclature that was used to describe the type III kerogen macerals belongs to the huminite group [34]. The macerals that were recognized during the organic petrography study are presented in Figure 3 and discussed below.

4.2.1. Huminite Macerals

Most commonly telohuminite sub-group macerals, such as textinite (intact and well-preserved cell walls with open cell-lumens), ulminite (massive/homogenized structured huminite particles with minor open cell-lumens) and finally texto-ulminite (intermediate phase of textinite and ulminite with collapsed walls and partly open cell-lumens filled occasionally by gelified material), were recognized. Attrinite (fragmental cell walls) was also often encountered, as well as corpohuminite (structureless bodies filling cell lumens) inside telohuminite macerals.

4.2.2. Inertinite Macerals

The inertinite group macerals were also very periodically encountered, especially fusinite (charred material/charcoal from forest fires and less often tissues with strongly bonded oxygen) and semifusinite (either partially charred material from forest fires as fusinite or humic material that was partially

oxidized by biochemical activity before or right after shallow burial). Funginite (material of fungal origin) and inertodetrinite (fragments) were also abundant.

4.2.3. Liptinite Macerals

Their abundance is very limited and they are not regularly present in comparison with the huminite and inertinite group macerals. They were recognized under blue-light excitation (500 nm), as they obtain yellowish fluorescence. The only liptinite maceral recognized was cutinite, which represents the outer walls of leaves, stems and other aerial parts of plants. As such, this maceral was resistant to degradation during sedimentary transport. Exceptionally solid bitumen (bituminite) may be found around silicates or inside the fracture porosity of large detrital grains.

With respect to the preservation status of the macerals, both opaque and non-opaque, biostructured and non-biostructured (banded and pitted) phytoclasts were recognized and classified according to [35].

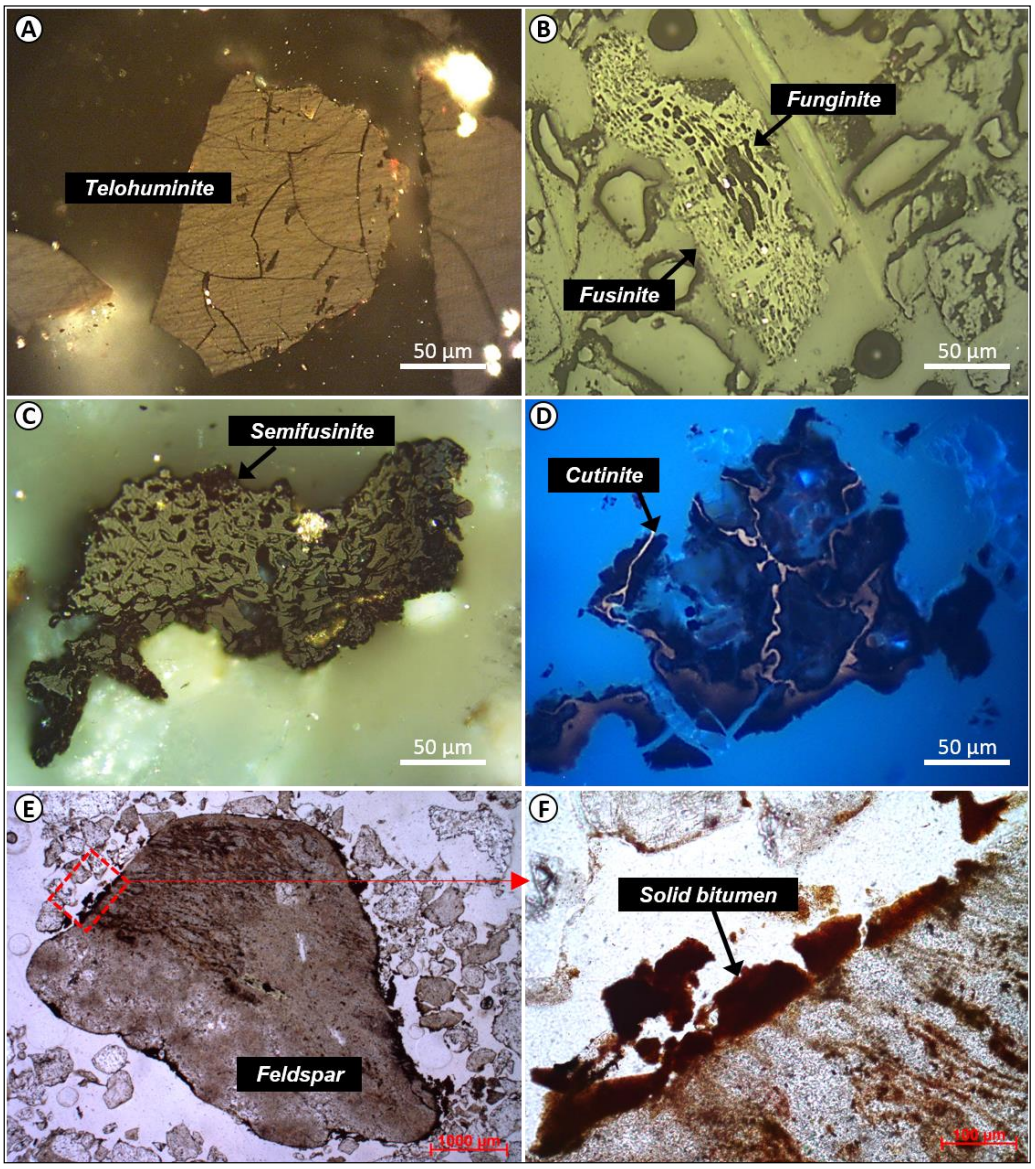

Figure 3. Presentation of the organic particles (macerals) recognized in the Zoovch Ovoo reservoir. (**A**–**C**) Polished blocks under oil-immersion indicating telohuminite, fusinite, funginite and finally semifusinite. (**D**) Fluorescence mode on thin section indicating cutinite. (**E**,**F**) Plain light on thin section showing solid bitumen penetrating and concentrated along the rims and fractures of a porous feldspar.

4.3. Petrography of Organic Matter—Uranium Associations and Mineral Geochemistry

Uranium mineral phases were studied by means of electron probe micro-analysis (Table 1) in samples of variable lithologies (e.g., matrix supported sandstones and sandstones cemented by dolomite), also discussed in [36]. Two phases were identified—uraninite and coffinite, sometimes occurring together. Uraninite forms independent spheres at a minimum size range of 1 µm, while Ca-P-rich coffinite occurs as elongated flakes of 12 µm size (Figure 4). Aggregates of the previous two oxides are also common. In both minerals, Ca, Si, P, Zr and Ti are contained in significant concentrations. The U + Ca versus Si binary plot (Figure 4) shows that the data points are distributed in-between the two end-members. The most abundant U mineral is uraninite (UO_2), slightly deviating from the stoichiometric formula due to P, Zr and Ti enrichment. The second and less common is Ca-P-rich coffinite [(U,Ca)(P,Si)O_4]. Pure coffinite is absent.

Table 1. Most representative values that are close to the end-members of uraninite and Ca-P-coffinite. Data obtained from EPMA (Electron Probe Microanalyser).

Oxides Mass (%)	Uraninite		Coffinite	
UO_2	76.28	76.48	61.92	56.58
SiO_2	1.20	1.30	6.65	12.69
P_2O_5	2.06	2.18	6.23	7.40
CaO	3.58	3.39	4.00	5.67
Total	83.12	83.35	78.80	82.34

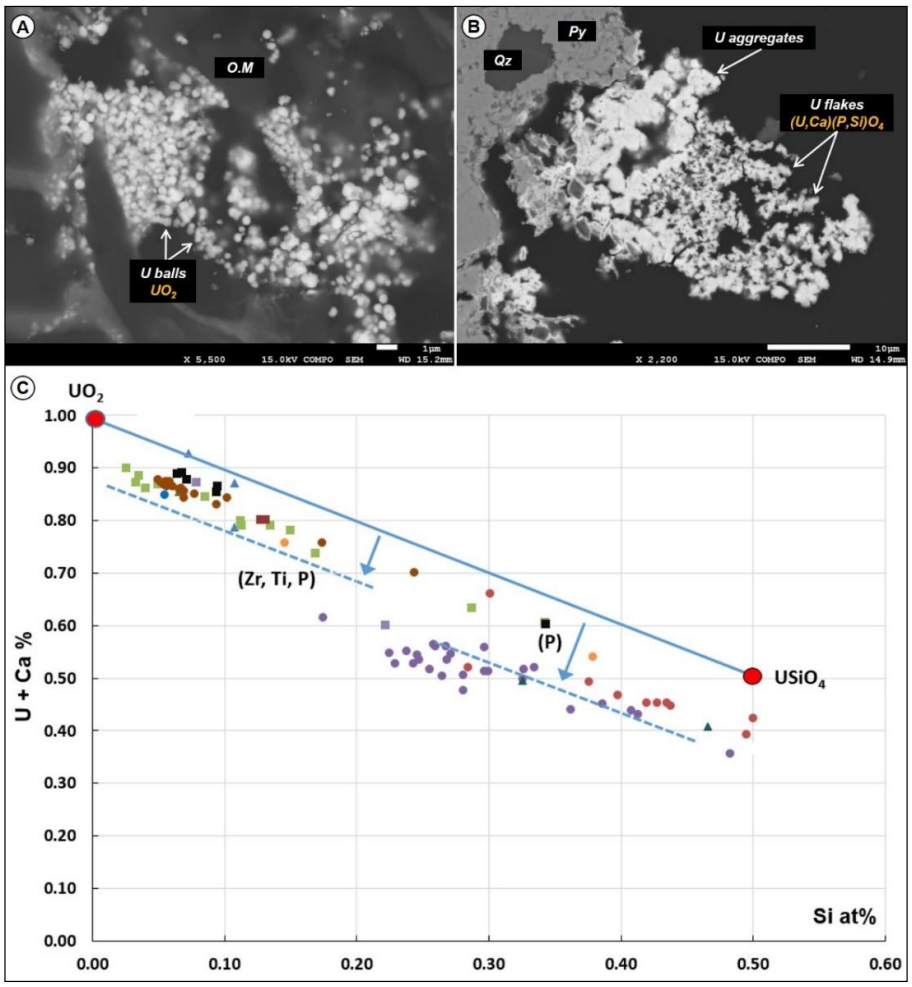

Figure 4. (**A**) SEM images of uraninite (U spheres) associated with organic matter and (**B**) Ca-P-coffinite (U flakes) associated with pyrite. Aggregates of both U minerals are also indicated. (**C**) Binary plot

of the U + Ca versus Si in at% oxide, indicating the stoichiometric U-mineral domains of uraninite, phosphorus-enriched uraninite, coffinite and phospho-coffinite, used as references (data from EPMA).

With the help of SEM-EDS and micro-XRF, it was possible to identify three different cases of uranium–organic matter associations, which are presented below.

4.3.1. U-Rich Organic Matter without any Distinguishable U-Phase

The organic particles in the Zoovch Ovoo sands often contain high concentrations of uranium. An assemblage of telohuminite and inertinite macerals, (i.e., texto-ulminite, corpohuminite and funginite) are illustrated in Figure 5. Half of the macerals are fully epigenetized by framboidal pyrite, while few contain pyritospheres at a very local scale. Based on the SEM-EDS concentration maps, corpohuminite is much richer in sulfur than texto-ulminite. Sulfur is nearly absent from funginite except for the rims. Iron content is constant in both huminite group macerals, while it is absent from funginite. Uranium occurs in higher concentrations in corpohuminite. Titanium is always present at a rather low concentration. In addition, some disseminated Ti-oxide grains were identified.

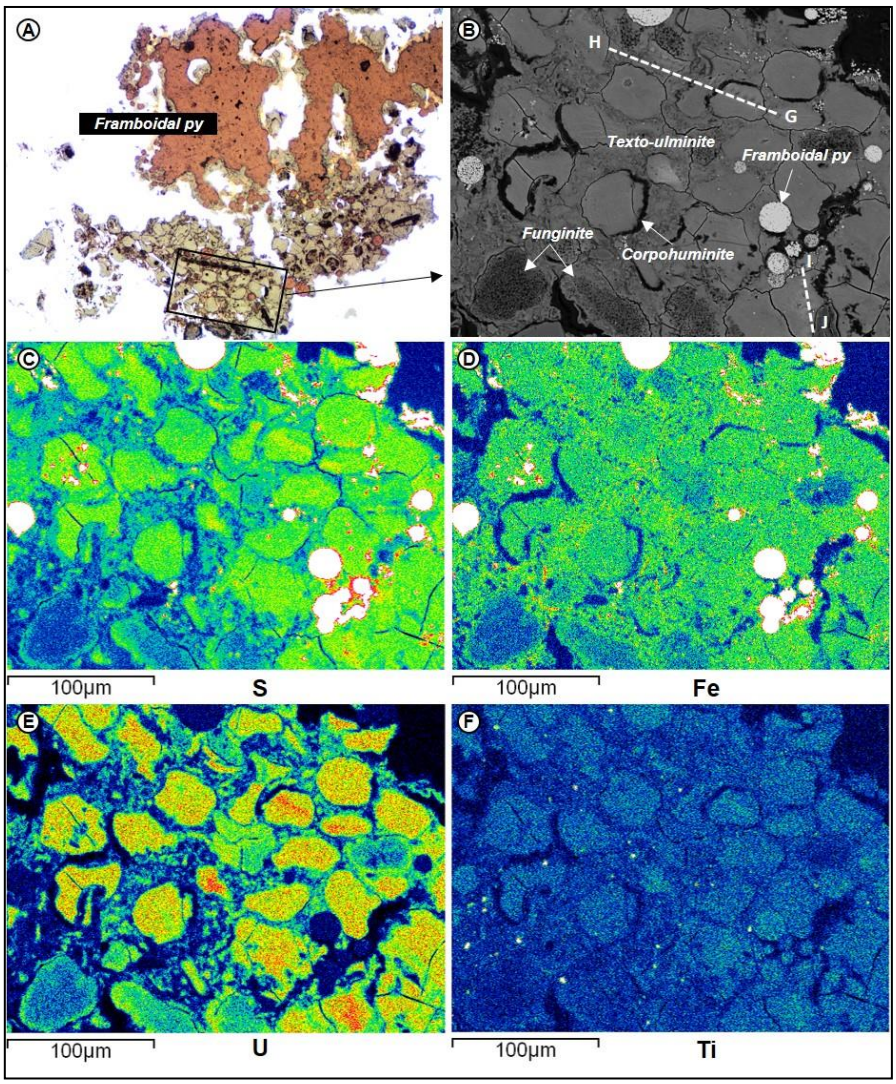

Figure 5. Organic matter relationships to U, Fe, S and Ti. The macerals corpohuminite, texto-ulminite and funginite are locally associated to framboidal pyrite (**A**) under reflected light and (**B**) in SEM mode. (**C**–**F**) The SEM-EDS maps for S, Fe, U and Ti suggest that sulfur and iron are present in all particles, showing a preference for corpohuminite, then for texto-ulminite and finally for funginite. Likewise,

the uranium concentration follows the same preference pattern. In some cases, certain corpohuminite particles are particularly enriched in U. Titanium is mainly dispersed at low concentrations in macerals, but is also contained as microsized Ti-oxides.

The concentrations of U, Fe, S and Ti of the two profiles G-H and I-J in Figure 5B are presented in Figure 6. Profile G-H includes both corpohuminite and texto-ulminite macerals, and shows that the corpohuminite contains up to 20 wt % U, while texto-ulminite fluctuates between 7 and 12 wt % U. For certain parts of the profile, S and Fe concentrations vary together, and indicate the presence of pyrite micro-crystals. In other parts, S and Fe are not perfectly correlated. Titanium concentration is nearly constant around 0.5 wt %. Profile I-J was performed strictly within a corpohuminite particle. Uranium concentration ranges between 16 and 22 wt %, S and Fe between 4 and 5 wt % while no visible optical expression of sulfide.

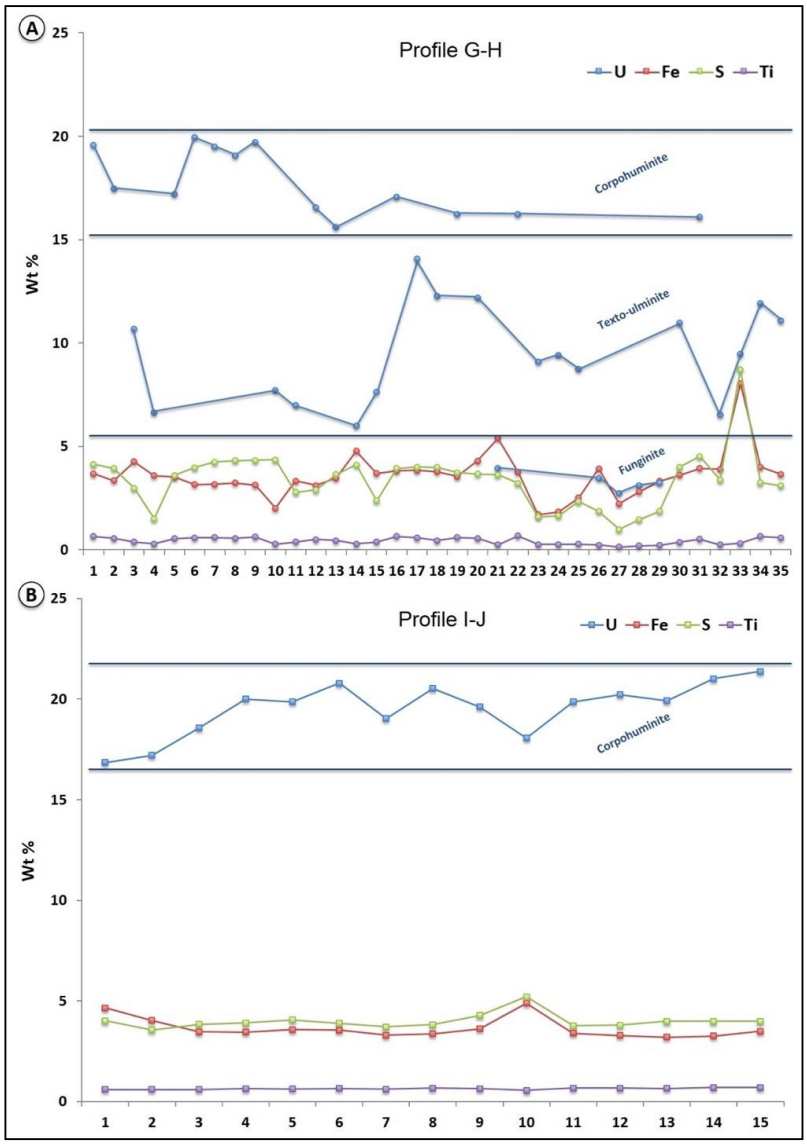

Figure 6. The profiles G-H and I-J presented in Figure 5. Profile G-H (**A**) indicates that the composition of uranium in corpohuminite is more than double that of the texto-ulminite background, reaching 19 wt %. Sulfur and iron concentrations are not perfectly correlated and several datapoints show antagonistic behavior. Profile I-J (**B**) was performed on a single corpohuminite particle and shows that uranium concentration is between 16 and 22 wt %. Sulfur and iron are sub-constant and correlated, which could be related to pyrite nanocrystal inclusions. Titanium is sub-constant and around 1 wt % for both profiles.

A binary plot for S and Fe (Figure 7) was constructed from the profiles G-H and I-J of Figures 5 and 6, with reference stoichiometry lines for pyrite (FeS_2) and amorphous FeS (e.g., mackinawite). Profile G-H refers to the transition between corpohuminite and texto-ulminite particles, showing Fe concentrations between 1.8 and 8.0 wt % while S fluctuates between 1.0 and 8.5 wt %. Most of the data points plot away of the pyrite composition reference line by approximately 2.0 wt % Fe. Some data points correspond to a slight enrichment in S from the reference line by a maximum of 1.5 wt %. Some data points distribute along the pyrite stoichiometry line, although there are clear deviations from the FeS_2 line towards the FeS line. In the profile I-J (corpohuminite), Fe concentration varies between 3.2 and 4.9 wt %, whereas S is between 3.5 and 5.1 wt %. Most of the data points are tightly plotted close to the FeS_2 line, which could indicate the presence of nanometric (<0.1 μm) pyrite inclusions similar to the data obtained from profile G-H.

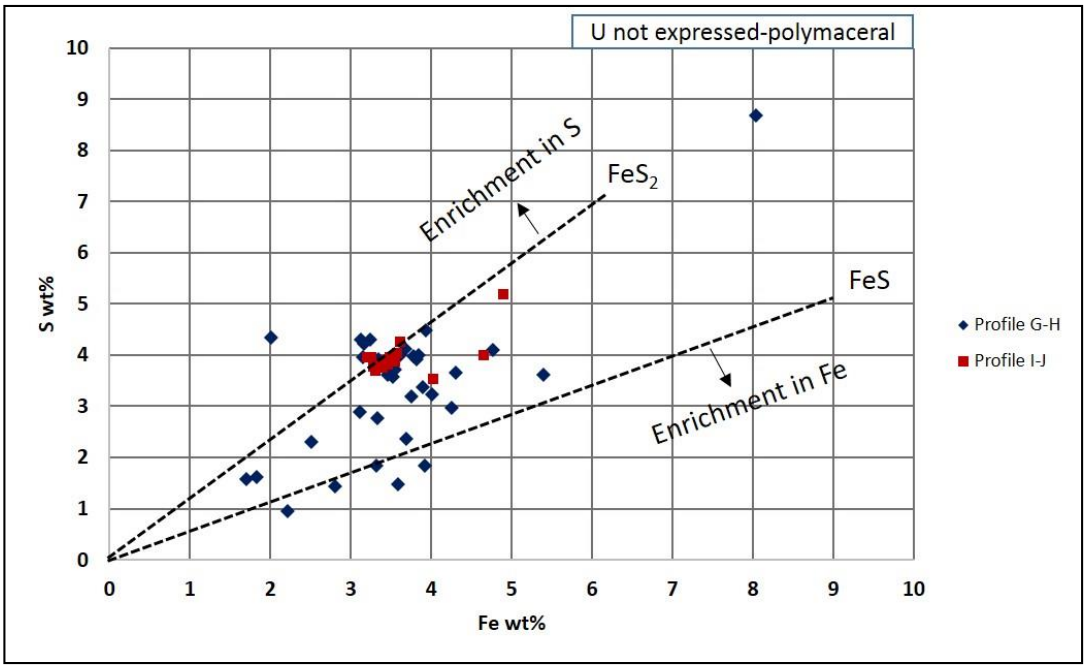

Figure 7. S–Fe binary plot, illustrating profiles G-H and I-J presented in Figure 5. Reference lines refer to the stoichiometry of FeS_2 (pyrite) and FeS (i.e., mackinawite).

A root structure composed of telohuminite macerals, particularly textinite to texto-ulminite, was also analyzed (Figure 8). The concentrations of U, Fe, S and Ti along the profile A-B of the root structure are presented in Figure 8C. The U concentrations are between 10 and 20 wt %. Sulfur concentrations fluctuate slightly around 2.5 wt %, but can reach 5.5 wt %, whereas iron is less than sulfur by approximately 1 wt %. Titanium is contained below 1.0 wt %. Profile C-D refers to the external part of the root. In this profile (not presented), the U concentration fluctuates between 15.0 and 3.0 wt %. Titanium concentration reaches 1.2 wt % at maximum.

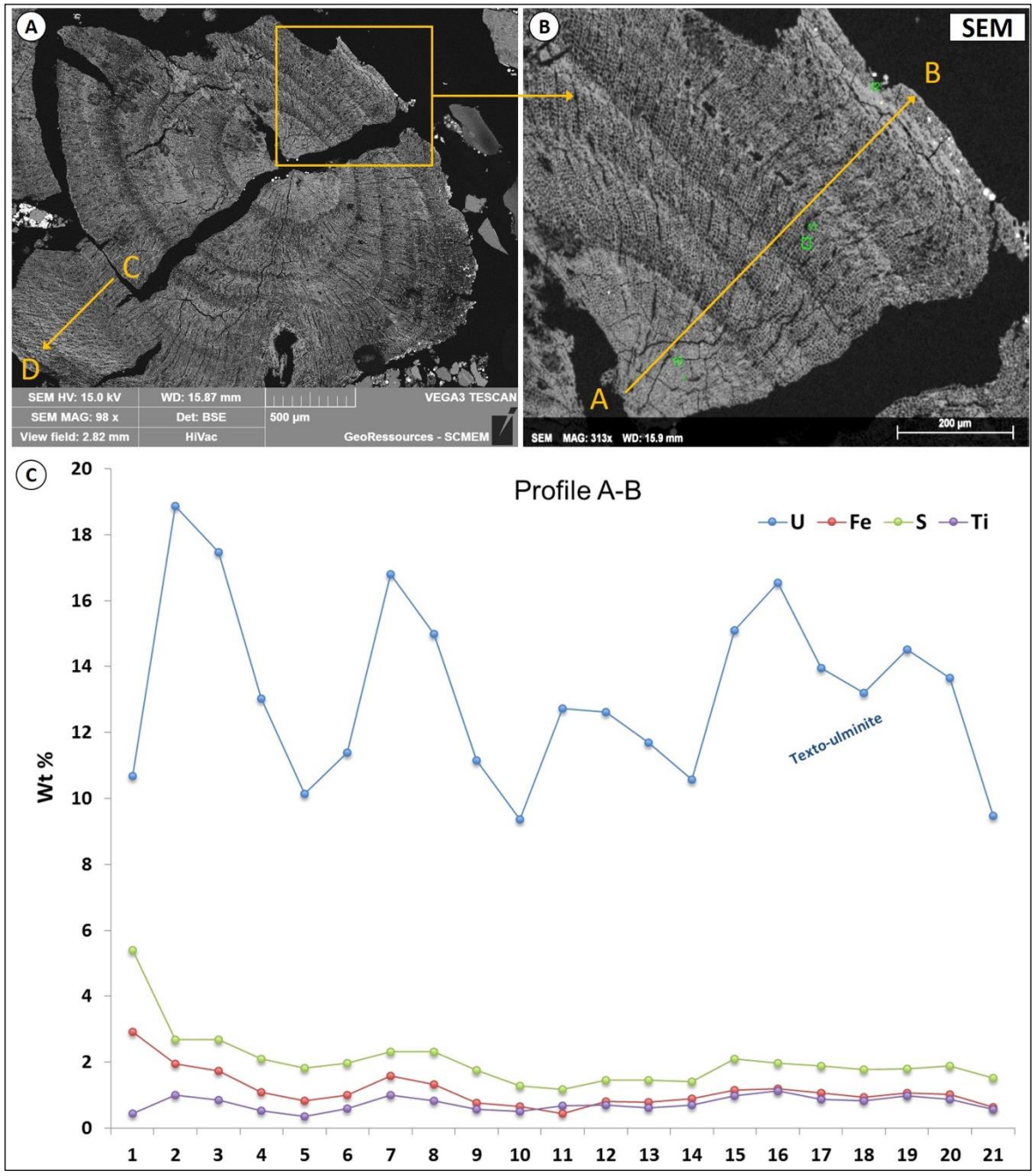

Figure 8. (**A**) View of a well-preserved root structure (telohuminite) typical of the organic matter contained in the Zoovch Ovoo sediments and the associated X-Ray microfluorescence maps. (**B**) Zoomed image of a part of the root highlighting the EPMA profile (A-B) for U, Fe, S, Si and Ti, respectively. (**C**) According to the EPMA profile of A-B performed on the root structure (texto-ulminite), S and Fe are always present inside the particle; however, their stoichiometry does not indicate pyrite. Titanium is also present in minute quantities (<1 wt %). Uranium concentration fluctuates between 10 and 19 wt %.

Sulfur and Fe concentrations along profiles A-B and C-D are projected on a binary plot (Figure 9). The Fe-S data points for the internal part (A-B) of the root are very close to pyrite stoichiometry. The profile (C-D) of the external part shows a trend enriched in Fe from 1 to 8 wt %, while S fluctuates between 0.5 and 2.8 wt %. Data points from both profiles indicate an enrichment in S up to 1 wt % compared to pyrite stoichiometry, while Fe enrichment may exceed mackinawite stoichiometry in profile C-D.

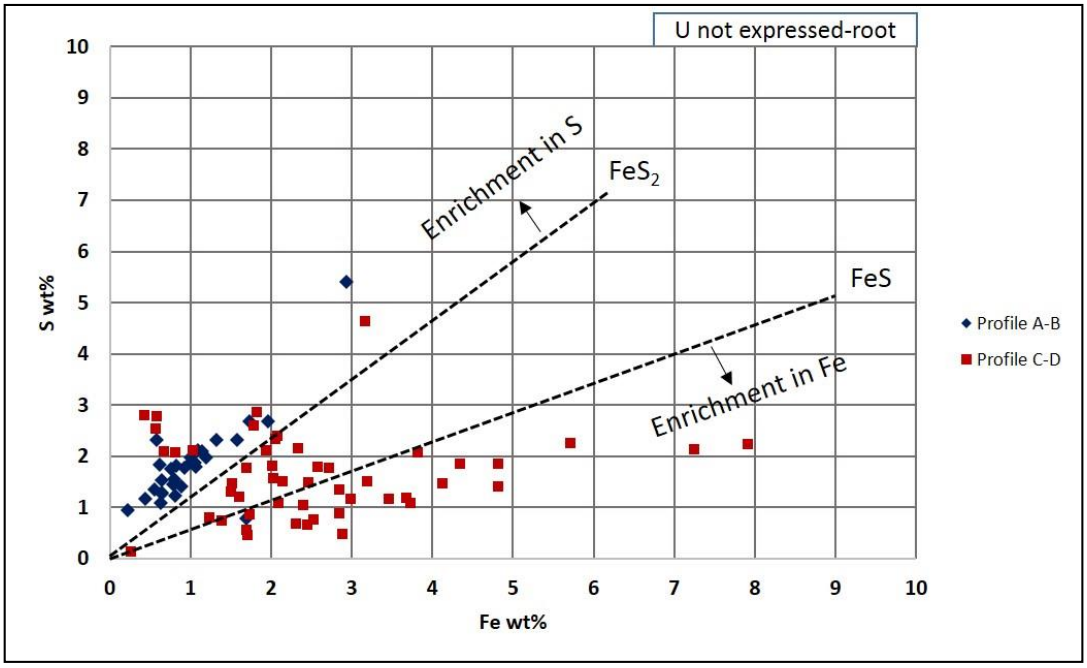

Figure 9. S-Fe wt % composition plot derived from the EPMA measurements along profiles A-B and C-D presented in Figure 8. Profile A-B was performed on the internal part of the root structure, whereas C-D was performed in the external part. For the internal part, the data points (in blue) distribute close to the pyrite line, with a slight relative S enrichment. For the external part, most data points in red indicate significant Fe enrichment at constant S concentration.

4.3.2. Uranium Oxides Precipitated at the Contact of the Organic Particle

UO_2 infillings occur most frequently around organic matter particles or within maceral micro-fractures, as confirmed by micro-XRF maps (Figure 10B). In the particle presented in Figure 10A, uranium concentration is rather low. There are two distinct distributions of Fe and S: (a) as pyrite micro-inclusions, observed under reflected light microscopy and confirmed by micro-XRF; and (b) as zones enriched either in Fe or S with the two elements not correlated (Figure 10C,D). In other examples, the U phases are distributed at the rim of organic particles (Figure 10E,F). If framboids were present in the organic matter before U epigenization, uranium may enter through the pore space of the micro-cubes that build-up the framboid and act as cement (Figure 10G). Sometimes when a telohuminite particle has large open pore spaces or fractures in the interior part, uranium oxides may precipitate there as well (Figure 10H).

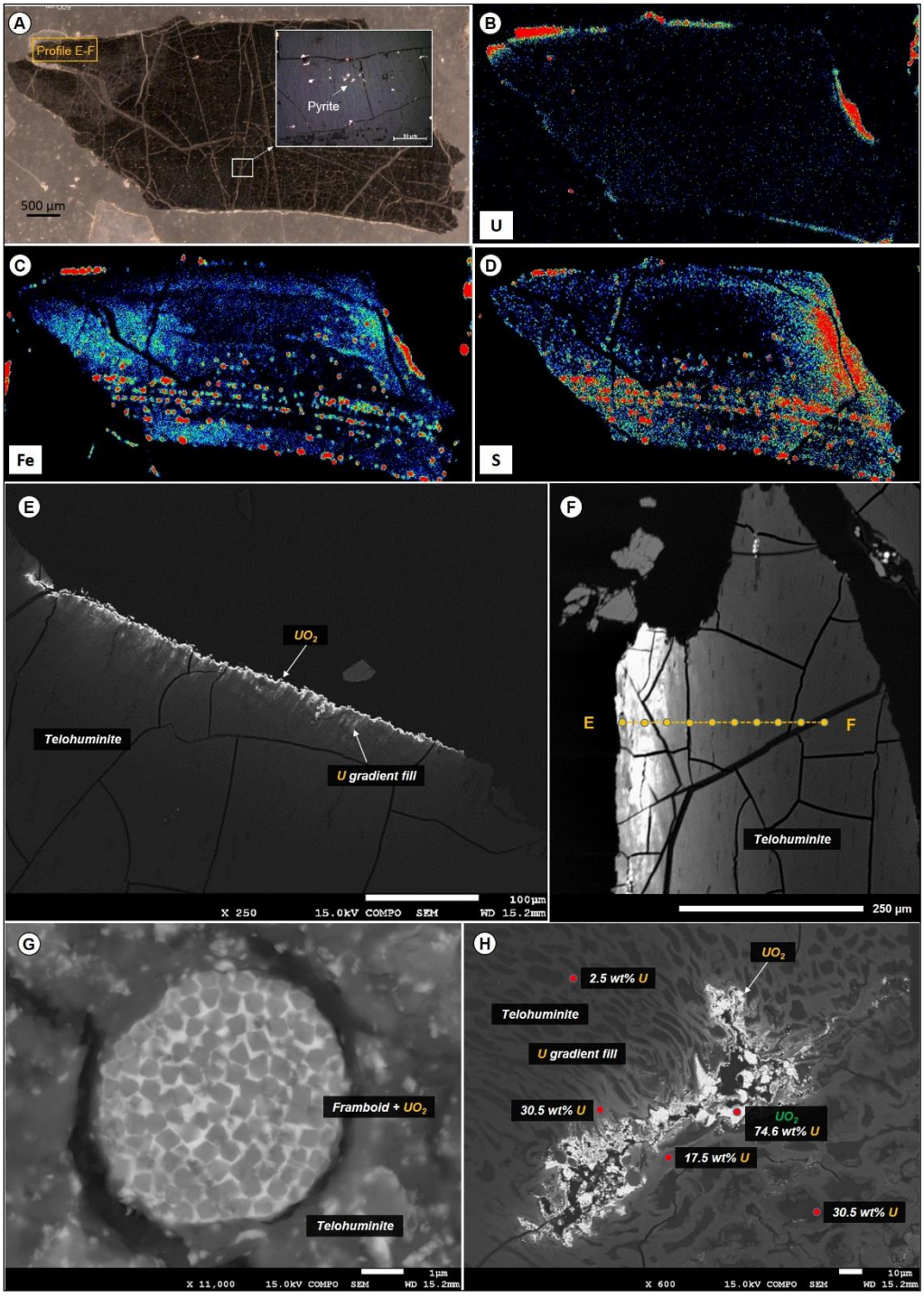

Figure 10. Telohuminite particle and the associated X-Ray microfluorescence maps. (**A**) Overview of the particle under reflected light, showing the EPMA profile position E-F for U, Fe, S and Ti, respectively, and a zoomed image showing the presence of pyrite. (**B**–**D**) The XRF maps for U, Fe and S. Uranium is highly concentrated around the rims and is much less abundant towards the interior of the particle. (**E**) BSE image showing uranium oxide precipitate (in this case UO_2) at the rim of a telohuminite particle. (**F**) The same association in higher magnification, coupled with an EPMA measurements profile (E-F/10 points), from the rim to the interior of the particle. (**G**) Uranium cement inside framboidal pyrite. (**H**) Uraninite precipitation along a fracture in the internal part of a telovitrinite/telohuminite particle. Uranium concentration decreases progressively from 74.6 to 2.5 wt % as a function of increasing distance from the fracture.

Uranium concentration along the fracture in the internal part of the telohuminite particle is typical of UO_2. Moving away from the fracture, the U concentration gradually decreases down to 2.5 wt %. It can be noted that a few percent (i.e., 3–5 wt %) of U inside the organic particles can significantly increase the average atomic number (Z) under BSE mode. Thus, the heterogeneous distribution of Z in an organic particle can reveal the U distribution.

The distribution of U, Fe, S and Ti for profile E-F covers a distance of about 300 µm from the rim, where there is UO_2 expression, towards the interior, where there is no visible mineral expression (Figure 11). Uranium concentration reaches about 20 wt % in the organic particle without being expressed as a visible phase and about 40 wt % when it is expressed as uraninite/Ca-P-coffinite. Sulfur, Fe and Ti are constantly below 0.5 wt %.

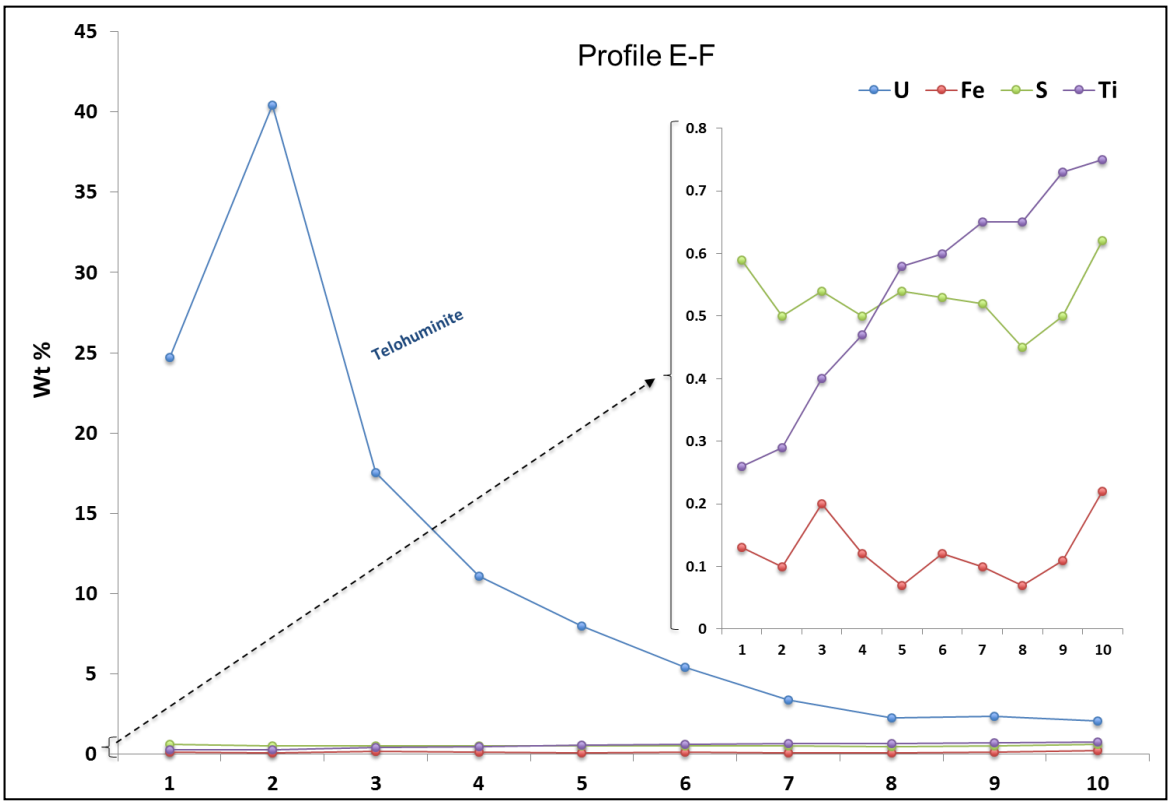

Figure 11. Profile E-F was performed on a telohuminite particle with uranium expressed as UO_2 at the rims. U concentration starts at 25 wt % at the rim. As shown in Figure 10F, the first point was measured on a part of the particle where UO_2 is not expressed as uraninite. The next spot was measured on a part where U is expressed as uraninite, hence the concentration is raised to 41 wt %. Afterwards the U concentrations decrease proportionally as a function of increasing distance from the particle rim. The Fe and S concentrations are at 0.1 and 0.5 wt %, respectively (with a detection limit of 0.1 wt %), as shown in the upscaled part of the graph. Titanium concentration increases from the rim towards the interior of the particle, from 0.26 to 0.75 wt %.

In the binary plot of S and Fe (Figure 12) it is clearly demonstrated that the telohuminite particle associated with U expressed as oxide at the rims is almost depleted for both sulfur and iron, though the data points are plotted very close to the FeS_2 line.

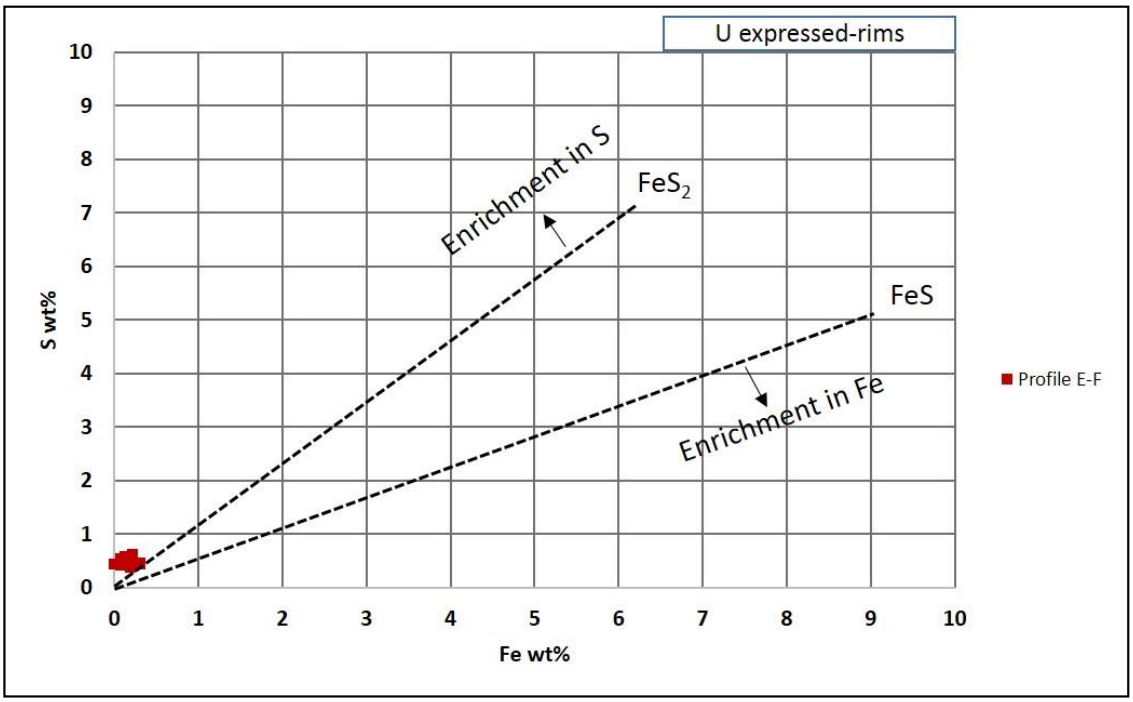

Figure 12. EPMA S and Fe concentration measurements of profile E-F performed on a telohuminite particle (ulminite). Both S and Fe are always below 1 wt %, with a slight enrichment in S. Reference lines refer to the stoichiometry of FeS_2 (pyrite) and FeS (i.e., mackinawite).

4.3.3. Uranium Phases Replacing Entirely Organic Matter

The UO_2 crystals progressively and almost entirely replace the organic carbon of the macerals. Based on the in situ SEM-EDS analyses the fully replaced particles contain macerals carrying more than 65 wt % U. This corresponds to the mix analysis of UO_2 and OM with approximately 20 wt % residual organic carbon. Fully replaced organic particles have 75–78 wt % U (Figure 13) with an additional few percent of Ca, Si and P.

It is also noted that even in the case of full organic matter replacement, some textural characteristics of the plant debris are preserved (i.e., cell walls and desiccation cracks), indicating fine-grained epigenization processes. Very often disseminated framboidal and euhedral pyrite is also present inside the U-replaced organic particle. Collapsed cell walls (attrinite) that are sometimes surrounding euhedral pyrite crystals can also be fully replaced by U, reaching 67 wt %, while becoming enriched in Ca, Si, and P. With progressive U epigenesis, even the macerals with minor permeability are replaced.

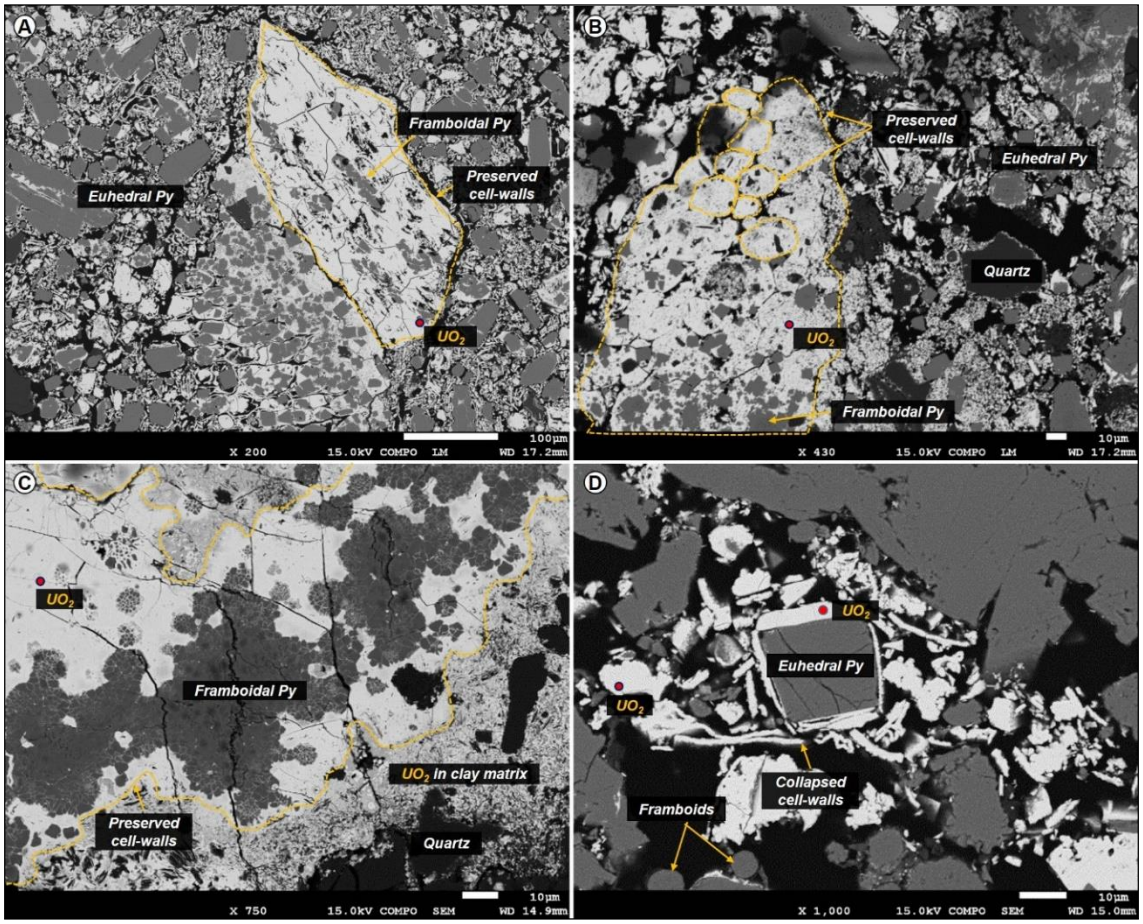

Figure 13. Examples of organic matter replaced by uranium, which is expressed in oxide form at the rims of the organic particle with a composition close to UO_2 stoichiometry (as measured under SEM-EDS mode). (**A**) Telohuminite particle at a size range of 400 µm, with the textural characteristics (cell walls and desiccation cracks) still visible. (**B**) Elongated telohuminite particle composed of smaller epigenetized corpohuminite particles. (**C**) A fully uranium-cemented organic particle associated with framboidal pyrite showing features of corrosion and uranium replacement. The cell walls of the particle are preserved even after replacement. The particle is surrounded by U-rich clay matrix. (**D**) Collapsed cell wall structures (attrinite) surrounding a large euhedral pyrite crystal.

5. Discussion

5.1. Detrital Organic Matter and U Distribution in Sediments

5.1.1. Origin of Organic Matter

According to sedimentological core analysis, peat and coal layers are absent inside the reservoir zone. The organic matter contained in the Zoovch Ovoo reservoir occurs as detrital particles, deposited according to the sedimentary bedding. Maceral analysis indicates that the organic particles are of higher plant origin, and can be found in either reduced (huminite group macerals) or oxidized (inertinite group macerals) states. The coarse, angular and poorly sorted organic particles are linked to distant transport (reworked) within high-energy flood-dominated depositional conditions, and associated with coarse- to medium-sized lithologies (coarse- to medium-coarse-grained sands). Organic matter particles encountered in fine clay layers are better preserved and linked to calm depositional conditions, except when they represent intraclasts distributed among the sand layers. The well-preserved phytoclasts, such as root remains associated with fine-grained organic-rich lithofacies, could be indicative of higher plants that grew within the depositional environment (e.g., no significant transport). Maceral

morphology ranges from intact to partially collapsed tissue, indicating that there is more than one organic matter source, and that the preservation stage of the maceral is directly linked to the distance from those sources. In principle, the more distal the source, the more fragmented/oxidized the organic particle that reaches the basin is [37]. Hence, it could be proposed that there are two main potential sources, a proximal for the well-preserved huminite group macerals, and a distal for the angular lath-shaped inertinite group macerals.

Bituminite represents an exception, and refers to liquid organic matter formed during vitrinite diagenesis (i.e., the coalification process that transforms peat stage material to higher rank coal) [38]. Bituminite is not abundant, and when present it was found located around or inside fracture porosity of large silicate grains (>0.5 mm size).

5.1.2. Uranium Uptake from Interstitial Waters

Dissolved uranium in surficial waters generally results from the dissolution of accessory minerals during weathering of the outcropping formations, and is transported as uranyl species in oxidizing media [39]. The processes of uranium–organic matter interactions in shallow buried sediments are complex and involve both processes of complexation and adsorption, followed by a reduction of the uranyl ion [4,8,16,40].

The process of chemical complexation was thoroughly described by [7,11]. Laboratory experiments showed that the complexation of uranium (without reduction) by the carboxyl groups of terrestrial organic matter is possible by forming uranyl–carboxyl compounds even at low temperatures (20–45 °C). They also showed that U(VI) reduction to U(IV) would require high temperatures (reaching 250 °C), which could be achieved either during late diagenesis or during hydrothermal conditions. However, not all terrestrial organic matter is able to form U complexes. It must be rich in oxygenated functions, particularly in carboxyl groups. Nakashima (1992) [7] studied two humic substances, one with a vitrinite reflectance of 0.50% (Gardanne lignite, Late Cretaceous) and another of 0.34% (Arjuzanx lignite, Late Miocene–Pliocene). The two lignite samples underwent the same laboratory procedure to test their potential to complex U at low temperatures from a U-rich fluid. It was proven that only the lignite of lower reflectance adsorbed uranyl cations (UO_2^{2+}) without reduction [41]. The complexation of uranyl resulted in pH increase, a decrease of UO_2^{2+} concentration and a simultaneous increase in H^+ as hydrogen was substituted and hence liberated from lignite by ion exchange. FT-IR (Fourier Transform Infrared Spectroscopy) analysis revealed that all along uranyl complexation, the carboxylic acids and ketonic groups (C=O) were progressively decreasing, whereas the aromatic groups (C=C and COO–) were increasing [11,42]. The conclusion was that the abundance of carboxylic functional groups in organic matter plays a major role in uranium complexation.

Another similar case of soluble U(VI) species fixed by lignite of low maturity resulting in the formation of UO_2^{2+} complexes was reported by [12], who studied lignite from the Coutras U-ore deposit, France. Though this immature lignite was never subjected to elevated temperatures, it can contain up to 19 wt % uranium without any distinguishable visible form.

From the above, it could be suggested that the lignite from Arjuzanx (Landes, France; Late Miocene or Pliocene; [7]) as well as the lignite from the Coutras (Gironde, France; Middle Eocene; [12]) could be used as direct analogues of the Zoovch Ovoo case, since they both demonstrate the same low level of maturity and have trapped uranium at low temperatures, between 20–45 °C (maximum burial temperature at Zoovch Ovoo is estimated at 40 °C according to [28,30,37]). The stage of chemical complexation of uranium without reduction uptaken by organic matter may be considered as the earliest stage of U concentration. Though deep burial is a priori excluded in Zoovch Ovoo, it is still difficult to know at which time the U enrichment of macerals occurred. Hence, there are two possible stages: (i) during sedimentation (syngenetic), and (ii) during the shallow burial of the sediments (early diagenetic).

5.1.3. Uranium Trapping Processes Involving Organic Matter at Zoovch Ovoo

Three factors seem to control the epigenization process of the macerals: (1) the permeability around the macerals, (2) the porosity of the macerals and (3) their chemical composition. The process is heterogeneous as the organic matter–uranium associations are not a function of the maceral group (i.e., huminite/vitrinite or inertinite), and all macerals from the same group have not undergone uranium epigenization.

Among the macerals, texto-ulminite (cell walls) and corpohuminite (filled cell walls) most often show high uranium concentration without expression of a visible U phase. In these macerals, the U concentration is rather homogeneous and reaches 15–20 wt %, which is similar to the 19 wt % described in [12], but higher than the 5 wt % reported in [43] and the 8 wt % in [44]. In particular, corpohuminite can host twice the concentration of U compared to adjacent texto-ulminite macerals. This feature is apparently linked to the chemistry of the macerals, and could be related to the abundance of carboxylic functional groups known to be responsible for U complexation [8,11,42]. The U speciation in these macerals could not be determined, as no U-bearing phase larger than the resolution of SEM (around 0.1 microns) could be observed. Meunier et al. (1990) [12] considers that U dispersed in organic matter occurs under its reduced state U(IV) and is probably in the form of small-sized U oxides.

Direct reduction by organic carbon is also likely to occur [45]. Nakashima et al. (1984) and Nakashima (1992) [7,11] suggest that aliphatic hydrocarbons may be involved in the reduction of U(VI). Yet, their experiments suggest that this mechanism is significant at T > 120 °C, which is not the range of temperatures experienced in the Zoovch Ovoo deposit.

Organic matter of low thermal maturity, like the one encountered in the Zoovch Ovoo deposit, can sustain microbiological activity [46–49]. Especially in the presence of sulfates, sulfate-reducing bacteria may be active and generate reduced sulfur species (i.e., H_2S/native sulfur) [50,51].

Another possibility of U reduction is the mechanism of biomineralization (by bacteria and fungi) previously studied by [46] and by [48] in laboratory experiments and in the case of Chinese roll-front systems, respectively. Both studies showed that during the mineralization stage it is possible to enzymatically reduce U into uraninite/coffinite by dissimilatory bacteria, which could use U(VI) as the sole electron acceptor instead of other multivalent metals such as Fe(III). Amorphous UO_2 may be the result of such processes. Indeed, besides complexation and sorption, a third mechanism was recently proposed by [52]: the formation of U(IV) biofilms that evolve into biogenic non-crystalline U(IV) compounds. Thus, using EXAFS (Extended X-ray Absorption Fine Structure) spectroscopy data, these authors revealed the role of microorganisms in the reduction of U(VI) and the formation of disseminated U(IV) in organic matter, acting both as nutrient and as trap.

For Zoovch Ovoo, the successive stages of uranium–organic matter epigenization are summarized in Figure 14. Most values for uranium concentration in organic matter range from 10–20 wt %. In that case, that the speciation of U is not known, since the size of the crystal, if present, would be lower than 0.1 µm. It was also observed that when U concentration reaches 40–45 wt %, UO_2 minerals will be present. The epigenization process is not the same for porous and non-porous macerals, hence two different pathways are proposed. In the case of non-porous macerals, for instance texto-ulminite with fully fused cell walls (Figure 10), the epigenization starts from the rims and internal fractures, if any are present. In the case of porous macerals (i.e., textinite (Figure 8) and funginite (Figure 5)) the epigenization will be more pervasive. The progressive accumulation continues until the particle is fully replaced (about 78 wt % U).

When an organic particle is composed of different macerals, the pores in-between the different macerals enhance fluid penetration, resulting in a more homogenous epigenization similar to what was described by [12]. In addition, it was observed that certain macerals (i.e., corpohuminite (Figure 5)) will accumulate uranium faster and in greater amounts than texto-ulminite or fusinite.

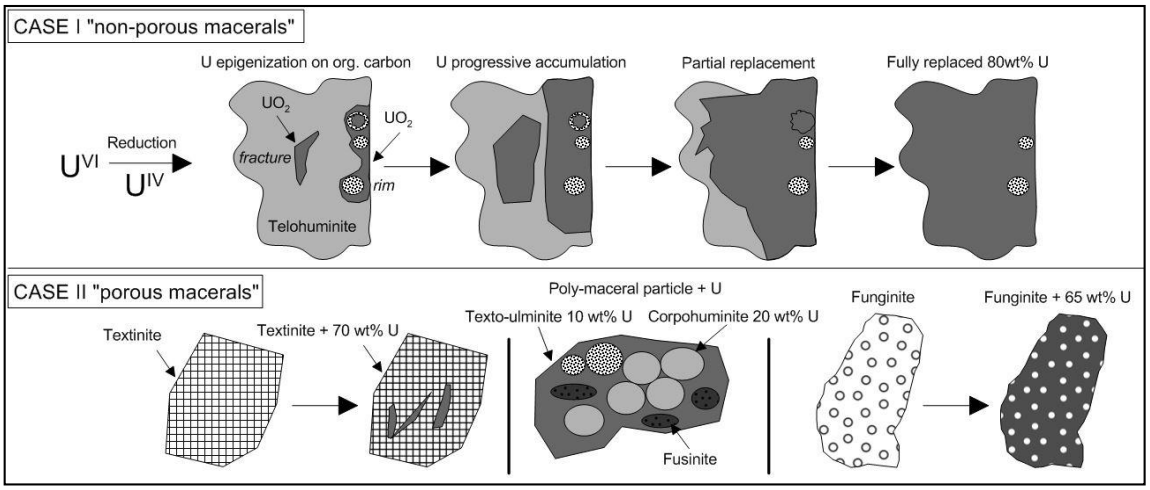

Figure 14. Graphical representation of organic matter epigenization by uranium. Uranium is carried in solution as U(VI) until it encounters a reducing agent and becomes U(IV). When uranium is reduced in the presence of macerals, it can be concentrated around internal fractures or at the rims of the maceral as uranium oxide. There is a linear decreasing concentration gradient from the rim where U is expressed as oxide towards the interior where no mineral form is visible. Eventually the replacement process keeps up, leading primarily to partial and progressively to full replacement (i.e., organic particles with up to 78 wt % U). One of the main aspects of this replacement process is that the fully replaced organic particle maintains its textural characteristics, although organic carbon is in very small quantities or no longer present.

5.1.4. Iron and Sulfur in Organic Matter Particles

The relative amounts of Fe and S approximately follow the stoichiometry of pyrite, although iron sulfides are not always visible on SEM images and micro-XRF maps. However, significant shifts in stoichiometric relationships are observed (Figure 7) and confirmed by the micro-XRF maps where some parts of the macerals are enriched in Fe and other in S. Meunier et al. (1990) [12] also referred to iron and sulfur organic compounds contained in natural organic matrices that were not linked to iron sulfides. Dichloromethane extraction of the samples, followed by gas chromatography-mass spectrometry, identified in some cases elemental sulfur, whose presence may be linked to sulfate-reducing bacteria. The redox state of iron (when not associated with sulfur) in the organic matter of the studied samples is not easy to determine, but in regards to the reducing environment (organic matter, reduced species of sulfur, U(IV) minerals) it is highly probable to be Fe(II). The Fe(II) may originate from the dissolution of detrital grains (e.g., biotite) or may arise from microbial activity (reduction of Fe(III) carried together with U(IV) by the mineralizing fluid).

Thus, when associated in stoichiometric proportions, iron and sulfur may reflect the presence of the amorphous phases, which are precursors to pyrite as disordered mackinawite of formula $Fe_2(HS)_4$ [53] or $Fe_3S_3(H_2O)_6$ [54], ordered mackinawite, and greigite Fe_3S_4 [55–57], as illustrated in Figure 7. This might explain the absence of identified pyrite crystals in the organic matter. Compositions consistent with pyrite stoichiometry may indeed be indicative of microcrystals. Hence, excess of iron or sulfur in the analysis may be linked to Fe(II) carboxylates as well as to S^0 adsorbed by organic matter.

5.1.5. Sedimentological Control of Organic Matter and Uranium Distribution

Uranium geochemical anomalies, as presented in Figure 2, are systematically associated with organic-rich layers or intraclast accumulations. The sediments accompanying the anomalies are usually very coarse to coarse. This feature suggests that the uranium-bearing fluid is initially controlled by permeability, migrating along the coarser part of the sand layers (and along layer boundaries; e.g., erosional surfaces). Detrital organic matter particle accumulations in the vicinity of these highly permeable layers will then act as a trap and participate in the complexation and reduction processes of

U(IV), as explained above. Since grain size of the sediments and organic matter distribution are of direct inheritance of the sedimentary depositional system, it could be suggested that the migration of the U-bearing fluids as well as the U trapping by the organic matter are under sedimentological control at core scale.

6. Conclusions

Very high levels of uranium concentration (a few percent up to 78 wt %) were found in the detrital organic matter of the Cretaceous sands from the Zoovch Ovoo deposit in Mongolia. Such concentration levels have never been reported to occur in the other roll-front U deposits from the large uranium province of Central Asia, which extends from Kazakhstan to China and Mongolia. This peculiarity posed the question of the role of organic matter in uranium deposits.

Petrographic as well as geochemical investigation of the maceral particles allows to propose the following:

- Organic matter present at Zoovch Ovoo is land plant derived, and occurs as detrital particles concentrated into clay layers, clay intraclasts or sandy laminae. Biological features of particles are more or less preserved, depending on their transportation (proximal or distal origin). Its thermal maturity is very low (peat to lignite stage; %Rr = 0.3).
- Maceral particles show high concentrations (up to 20 wt %) of U not expressed as oxide (detectable under SEM). It is very likely that U(VI) is adsorbed as uranyl–carboxyl groups. The organic matter particles have therefore captured U from circulating fluids at a low temperature (T < 40 °C). It is not yet clear if the trapping occurred during sedimentation (pre-concentration stage), during the roll-front events or both.
- The land plant particles concentrated microbiological activity, which triggered biodegradation as well as iron and bacterial sulfate reduction. The absence of detectable pyrite crystals in the organic matter, despite the presence of Fe and S in often non-FeS_2 stoichiometric proportions, suggests the presence of other forms of sulfur, such as amorphous FeS phase (e.g., mackinawite) and/or elemental sulfur.
- The distribution of UO_2 in the organic particles seems to be linked to porosity/permeability of the organic structure, which may be a control of fluid accessibility to the macerals. Organic matter particles can be fully replaced by UO_2, with partial preservation of organic structure (suggesting an epigenesis).
- As burial diagenesis is too low to consider reduction of U(VI) by carbonaceous moieties, it is suggested that microorganisms are mainly responsible for the reduction of U(VI), either directly through their physiological activity, or by providing reduced sulfur, which is an efficient reducing agent for U(VI). Furthermore, Fe(II) carboxylates may also be considered as a possible reducing agent [58]. The U(IV) speciation can be better understood by using EXAFS. Thus, it is necessary to identify the potential presence of biogenic non-crystalline U(IV) compounds within the macerals.

From this study it may therefore be concluded that at least two controls of different scales can be considered for the Zoovch Ovoo uranium deposit:

1. At the scale of the sedimentary particles, organic matter plays a capital role in uranium deposition, as it acts as a uranium trap through complexation and sustains the U(VI) reduction mechanism into UO_2 through biological activity.
2. At the scale of the sedimentary deposit, organic matter distribution as well as the permeability network that allows the circulation of uranium-bearing fluids are controlled by the sedimentary architecture.

Author Contributions: Conceptualization, D.R., R.M. and M.C.; Methodology and data curation, D.R., R.M. and M.C.; Validation, M.B. and O.P.; Writing—original draft preparation, D.R.; Writing—review & editing, D.R., R.M., M.B., O.P. and M.C.

Funding: This work was performed and funded in the research framework between ORANO Mining and CREGU (Centre de Recherches sur la Géologie des Matières Premières Minérales et Energétiques), in the Laboratory of GeoRessources in Nancy, France.

Acknowledgments: We are grateful to COGEGOBI's geological team for the hospitality and equipment provided during the field work, as well as for taking care of the shipping of the samples from Mongolia to France. People from the laboratory of GeoRessources, in particular Andreï Lecomte and Olivier Rouer, are acknowledged for the crystal chemistry analyses and the manipulation of the analytical means. The MicroXRF used is an equipment co-funded by ICEEL (Carnot institute)-CREGU-Labex Resources 21 (reference ANR-10-LABX 21-LABEX RESSOURCES 21) and FEDER. Mrs. Jessica Strydom is acknowledged for her English grammar and syntactic revisions within the manuscript. Finally, the authors would like to thank both anonymous reviewers for improving the article.

Conflicts of Interest: The authors declare no conflict of interest.

References

1. Nash, J.T.; Granger, H.C.; Adams, S.S. *Geology and Concepts of Genesis of Important Types of Uranium Deposits*; Economic Geology Publishing Company: New Haven, CT, USA, 1981; pp. 63–116. [CrossRef]
2. Meunier, J.D.; Landais, P.; Monthioux, M.; Pagel, M. Oxidation reduction processes in the genesis of the uranium-vanadium tabular deposits of the Cottonwood Wash mining area (Utah, USA): Evidence from petrological study and organic matter analysis. *Bull. Minéral.* **1987**, *110*, 145–156. [CrossRef]
3. Landais, P.; Connan, J.; Dereppe, J.M.; George, E.; Meunier, J.D.; Monthioux, M.; Pagel, M.; Pironon, J.; Poty, B. Alterations of the organic matter, a clue for uranium ore genesis. *Uranium* **1987**, *3*, 307–342.
4. Landais, P. Organic geochemistry of sedimentary uranium ore deposits. *Ore Geol. Rev.* **1996**, *11*, 33–51. [CrossRef]
5. Spirakis, C.S. The roles of organic matter in the formation of uranium deposits in sedimentary rocks. *Ore Geol. Rev.* **1996**, *11*, 53–69. [CrossRef]
6. Cuney, M. Ore deposits, 2007. In *Encyclopedia of Geochemistry*; Springer International Publishing AG: Berlin, Germany, 2016; 13p. [CrossRef]
7. Nakashima, S. Complexation and reduction of uranium by lignite. *Sci. Total Environ.* **1992**, *117–118*, 425–437. [CrossRef]
8. Cumberland, S.A.; Etschmann, B.; Brugger, J.; Douglas, G.; Evans, K.; Fisher, L.; Kappen, P.; Moreau, J.W. Characterization of uranium redox state in organic-rich Eocene sediments. *Chemosphere* **2018**, *194*, 602–613. [CrossRef] [PubMed]
9. Anderson, R.F. Redox behavior of uranium in an anoxic marine basin. *Uranium* **1987**, *3*, 145–164.
10. Goldhaber, M.B.; Hemingway, B.S.; Mohagheghi, A.; Reynolds, R.L.; Northrop, H.R. Origin of coffinite in sedimentary rocks by a sequential adsorption-reduction mechanism. *Bulletin de la Société de l'industrie Minérale* **1987**, *110*, 131–144. [CrossRef]
11. Nakashima, S.; Disnar, J.R.; Perruchot, A.; Trichet, J. Experimental study of mechanisms of fixation and reduction of uranium by sedimentary organic matter under diagenetic or hydrothermal conditions. *Geochim. Cosmochim. Acta* **1984**, *48*, 2321–2329. [CrossRef]
12. Meunier, J.D.; Landais, P.; Pagel, M. Experimental evidence of uraninite formation from diagenesis of uranium-rich organic matter. *Geochim. Cosmochim. Acta* **1990**, *54*, 809–817. [CrossRef]
13. Van Krevelen, D.W. *Coal Typology–Chemistry–Physics–Constitution*, 1st ed.; Elsevier: Amsterdam, The Netherlands, 1961; 514p.
14. Tissot, B.P.; Welte, D.H. *Petroleum Formation and Occurrence*, 2nd ed.; Springer: Berlin/Heildelberg, Germany; New York, NY, USA, 1984; 699p.
15. Adreyef, P.F.; Chumachenko, A.P. Reduction of uranium by natural organic substances. *Geokhimiya* **1964**, *1*, 12–22.
16. Forbes, P.; Landais, P.; Bertrand, P.; Brosse, E.; Espitalié, J.; Yahaya, M. Chemical transformations of type-III organic matter associated with the Akouta uranium deposit (Niger): Geological implications. *Chem. Geol.* **1988**, *71*, 267–282. [CrossRef]
17. Granger, H.C.; Warren, C.G. Unstable sulfur compounds and the origin of roll-front type uranium deposits. *Econ. Geol.* **1969**, *64*, 160–171. [CrossRef]
18. Boulègue, J. Simultaneous Determination of Sulfide, Polysulfides and Thiosulfat as an Aid to Ore Exploration. *Dev. Econ. Geol.* **1981**, *15*, 21–36. [CrossRef]

19. Petrov, N.N. Les gisements épigénétiques du Kazakhstan. *Géologie du Kazakhstan* **1998**, *2*, 22–39.
20. Munara, A. Formation des gisements d'uranium de type roll: Approche minéralogique et géochimique du gisement uranifère de Muyunkum (Bassin de Chu-Sarysu, Kazakhstan). Ph.D. Thesis, Henri Poincaré University, Nancy, France, 9 July 2012; 327p.
21. Lach, P.; Cathelineau, M.; Brouand, M.; Fiet, N. In-situ isotopic and chemical study of pyrite from Chu-Sarysu (Kazakhstan) roll-front uranium deposit. *Procedia Earth Planet. Sci.* **2015**, *13*, 207–210. [CrossRef]
22. Cai, C.; Dong, H.; Li, H.; Xiao, X.; Ou, G.; Zhang, C. Mineralogical and geochemical evidence for coupled bacterial uranium mineralization and hydrocarbon oxidation in the Shashagetai deposit, NW China. *Chem. Geol.* **2007**, *236*, 167–179. [CrossRef]
23. Zhu, M.; Wu, R.; Liu, X.; Nie, F.; Yu, D. Geologic Setting of Interformational Braided Channel Type Sandstone Uranium Deposits in North China, East China Institute of Technology, 2012. Available online: https://www.slideshare.net/monatom/05-xiaodong-liu-geologic-setting-of-interformationalbraidedchannel-type-sandstone-uranium-deposits-in-north-china (accessed on 17 May 2019).
24. Yue, S.; Wang, G. Relationship between the hydrogeochemical environment and sandstone-type uranium mineralization in the Ili basin, China. *Appl. Geochem.* **2011**, *26*, 133–139. [CrossRef]
25. Bonnetti, C.; Cuney, M.; Malartre, F.; Michels, R.; Liu, X.; Peng, Y. The Nuheting Deposit, Erlian Basin, China: Synsedimentary vs. Diagenetic Uranium Mineralization. *Ore Geol. Rev.* **2015**, *69*, 118–139. [CrossRef]
26. Le Goux, F.; Banzragch, T.O.; Delaunay, A.; Nyamdorj, B.I.; Jaques, E.; Korshunov, A.; Parize, O.; Brouand, M. The Major Gobi Uranium Deposits, Upper Cretaceous East Gobi Basin, Mongolia: Geodynamical and Mineralogical Key Parameters of Uranium Ore Geology. In Proceedings of the 13th SGA Biennial Meeting, Nancy, France, 24–27 August 2015; Volume 5, pp. 1815–1818.
27. Dahlkamp, F.J. *Uranium Deposits of the World: Asia*; Springer: Berlin/Heidelberg, Germany, 2009; 493p.
28. Graham, S.A.; Hendrix, M.S.; Johnson, C.L.; Badamgarav, D.; Badarch, G.; Amory, J.; Porter, M.; Barsbold, R.; Webb, L.E.; Hacker, B.R. Sedimentary record and tectonic implications of Mesozoic rifting in southeast Mongolia. *Geol. Soc. Am. Bull.* **2001**, *113*, 1560–1579. [CrossRef]
29. Johnson, C.L. Polyphase evolution of the East Gobi basin: Sedimentary and structural records of Mesozoic-Cenozoic intraplate deformation in Mongolia. *Basin Res.* **2004**, *16*, 79–99. [CrossRef]
30. Prost, G.L. Tectonics and hydrocarbon systems of the East Gobi basin, Mongolia. *Am. Assoc. Pet. Geol. Bull.* **2004**, *88*, 483–513. [CrossRef]
31. Pontolillo, J.; Stanton, R.W. Coal Petrographic Laboratory Procedures and Safety Manual II. Open-File Report 94-631. U.S Department of Interior Geological Survey, 1994; 74p. Available online: https://pubs.usgs.gov/of/1994/0631/report.pdf (accessed on 4 September 2017).
32. (ISO) 7404-2. *International Organization for Standardization. Methods for the Petrographic Analysis of Coals—Part 2: Methods of Preparing Coal Samples*; International Organization for Standardization: Geneva, Switzerland, 2009; 12p.
33. (ISO) 7404-5. *International Organization for Standardization. Methods for the Petrographic Analysis of Coal—Part 5: Methods of Determining Microscopically the Reflectance of Vitrinite*; International Organization for Standardization: Geneva, Switzerland, 2009; 14p.
34. Sýkorová, I.; Pickel, W.; Christanis, K.; Wolf, M.; Taylor, G.H.; Flores, D. Classification of huminite—ICCP System 1994. *Int. J. Coal Geol.* **2005**, *62*, 85–106. [CrossRef]
35. International Committee for Coal and Organic Petrology (ICCP). *ICCP Training Course on Dispersed Organic Matter*; International Committee for Coal and Organic Petrology (ICCP): Porto, Portugal, 2011; 322p, ISBN 978-989-8265-67-8.
36. Rallakis, D.; Michels, R.; Brouand, M.; Parize, O.; Cathelineau, M. Dolomite cements in Cenomanian continental sand deposits: Time evolution and significance (Zoovch Ovoo, U-deposit, East Gobi Basin, Mongolia). *J. Sediment. Res.* **2019**. under review.
37. Borrego, A.G.; Cook, A. Humic Macerals: Vitrinite/Inertinite, Chapter 9. In *10th ICCP Training Course on Dispersed Organic Matter. Integrating Transmitted and Reflected Light Microscopy*; GFZ: Potsdam, Germany, 2017; 276p.
38. Van Krevelen, D.W. *Coal*, 3rd ed.; Elsevier: Amsterdam, The Netherlands, 1993.
39. Langmuir, D. Uranium solution-mineral equilibria at low temperatures with applications to sedimentary ore deposits. *Geochim. Cosmochim. Acta* **1978**, *44*, 1753–1766. [CrossRef]

40. Bone, E.S.; Dynes, J.J.; Cliff, J.; Bargar, J. Uranium (IV) adsorption by natural organic matter in anoxic sediments. *Proc. Natl. Acad. Sci. USA* **2017**, *114*, 711–716. [CrossRef] [PubMed]
41. Nakashima, S.; Disnar, J.R.; Perruchot, A. Precipitation Kinetics of Uranium by Sedimentary Organic Matter under Diagenetic and Hydrothermal Conditions. *Econ. Geol.* **1999**, *94*, 993–1006. [CrossRef]
42. Stevenson, F.J. *Humus, Chemistry. Genesis, Composition, Reactions*; John Wiley and Sons: New York, NY, USA, 1982; p. 443.
43. Douglas, G.B.; Butt, C.R.M.; Gray, D.J. Geology, geochemistry and mineralogy of the lignite-hosted Ambassador palaeochannel uranium and multi-element deposit, Gunbarrel Basin, Western Australia. *Miner. Depos.* **2011**, *46*, 761–787. [CrossRef]
44. Bonnetti, C.; Liu, X.; Zhaobin, Y.; Cuney, M.; Michels, R.; Malartre, F.; Mercadier, J.; Cai, J. Coupled uranium mineralization and bacterial sulphate reduction for the genesis of the Baxingtu sandstone-hosted U deposit, SW Songliao Basin, NE China. *Ore Geol. Rev.* **2017**, *82*, 108–129. [CrossRef]
45. Rouzaud, J.N.; Oberlin, A.; Trichet, J. Interaction of uranium and organic matter in uraniferous sediments. In *Advances in Organic Geochemistry*; Douglas, A.G., Maxwell, J.R., Eds.; Pergamon Press: Oxford, UK, 1979; pp. 505–516. [CrossRef]
46. Lovley, D.R.; Phillips, E.J.P.; Gorby, Y.A.; Landa, E.R. Microbial reduction of uranium. *Nature* **1991**, *350*, 413–416. [CrossRef]
47. Detmers, J.; Schulte, U.; Strauss, J.; Kuever, J. Sulfate Reduction at a Lignite Seam: Microbial Abundance and Activity. *Microb. Ecol.* **2001**, *42*, 238–247. [CrossRef] [PubMed]
48. Min, M.; Xu, H.; Chen, J.; Fayek, M. Evidence of uranium biomineralization in sandstone-hosted roll-front uranium deposits, northwestern China. *Ore Geol. Rev.* **2005**, *26*, 198–206. [CrossRef]
49. Menor-Salván, C.; Tornos, F.; Fernández-Remolar, D.; Amils, R. Association between catastrophic paleovegetation changes during Devonian-Carboniferous boundary and the formation of giant massive sulfide deposits. *Earth Planet. Sci. Lett.* **2010**, *299*, 398–408. [CrossRef]
50. Gruner, J.W. Syntheses of uranium minerals at room and elevated temperatures. *Am. Mineral.* **1953**, *38*, 342.
51. Kochenov, A.V.; Korolev, K.G.; Dubinchuk, V.T.; Medvelev, Y.L. Experimental data on the conditions of precipitation of uranium from aqueous solutions. *Geochem. Int.* **1977**, *14*, 82–87.
52. Bhattacharyya, A.; Campbell, K.M.; Kelly, S.D.; Roebbert, Y.; Weyer, S.; Bernier-Latmani, R.; Borch, T. Biogenic non-crystalline $U^{(IV)}$ revealed as major component in uranium ore deposits. *Nat. Commun.* **2017**, *8*. [CrossRef] [PubMed]
53. Davison, W.; Buffle, J.; Devitre, R. Voltammetric characterization of a dissolved iron sulfide species by laboratroy and field studies. *Anal. Chim. Acta* **1998**, *377*, 193–203. [CrossRef]
54. Theberge, S.; Luther, G.W. Determination of the electrochemical properties of a soluble aqueous FeS species present in sulfide solutions. *Aquat. Geochem.* **1987**, *3*, 191–211. [CrossRef]
55. Rickard, D.; Griffith, A.; Oldroyd, A.; Butler, I.B.; Lopez-Caper, E.; Manning, D.A.C.; Apperley, D.C. The composition of nanoparticulate mackinawite, tetragonal iron (II) monosulfide. *Chem. Geol.* **2006**, *235*, 286–298. [CrossRef]
56. Wolthers, M.; Charlet, L.; van Der Linde, P.; Rickard, D.; van Der Weijden, C. Surface chemistry of disordered mackinawite (FeS). *Geochim. Cosmochim. Acta* **2005**, *69*, 3469–3481. [CrossRef]
57. Bura-Nakić, E.; Viollier, E.; Jézéquel, D.; Thiam, A.; Ciglenečki, I. Reduced sulfur and iron species in anoxic water column of meromictic crater Lake Pavin (Massif Central, France). *Chem. Geol.* **2009**, *266*, 311–317. [CrossRef]
58. Boyanov, M.I.; O'Loughlin, E.J.; Roden, E.E.; Fein, J.B.; Kemner, K.M. Adsorption of Fe(II) and U(VI) to carboxyl-functionalized microspheres: The influence of speciation on uranyl reduction studied by titration and XAFS. *Geochim. Cosmochim. Acta* **2007**, *71*, 1898–1912. [CrossRef]